Set-up of a generic aeroelastic simulation model for demonstration and software testing purposes

Francisco Carvalho[1*], Arne Voß[2] and Raffaello Mariani[1]

[1*]Aerospace, Moveability and Naval Architecture, KTH Royal Institute of Technology, Stockholm, Sweden.
[2]Loads Analysis and Design Department, DLR - German Aerospace Center, Institute of Aeroelasticity, Göttingen,Germany.

*Corresponding author(s). E-mail(s): franciscomcpbcarvalho@gmail.com;
Contributing authors: arne.voss@dlr.de; rmariani@kth.se;

Abstract

This work presents the development and comprehensive analysis of an open-source aeroelastic model for the Douglas DC-3 with some modifications. The model serves as a platform for software testing, capturing essential aeroelastic phenomena. It features a conventional configuration with two engines, control surfaces, and a wing with a leading-edge sweep angle of 15.5°, dihedral angle of 5°, aspect ratio of 9.2, and cambered airfoil, operating in a subsonic regime. The development process included finite element modeling using beam elements, aerodynamic modeling with the Doublet Lattice Method (DLM), and mass modeling, including a complex fuel mass model. Four distinct mass configurations were analyzed. Trim case analyses were performed using both *Loads Kernel* and SOL144 in *MSC Nastran*, revealing significant differences between rigid and flexible configurations. Maneuver load analyses were conducted exclusively using *Loads Kernel*. Additionally, gust loads were studied using the (1-cos) Discrete Gust Model, demonstrating coupling with the short-period mode due to high static margin. Flutter checks showed matching results between *Loads Kernel* and *MSC Nastran*, with flutter speeds of 195 m/s and 203 m/s, respectively, confirming the model's plausibility for aeroelastic analysis.

Keywords: Aeroelasticity, Douglas DC-3, Finite Element Modeling, Doublet Lattice Method, Trim Analysis, Maneuver Loads, Gust Loads, Flutter Analysis

1 Motivation and Introduction

The sparseness of open-source generic aeroelastic simulation models poses a significant challenge, as existing options are invariably held back by limitations. It is imperative, particularly for purposes of demonstration and software testing, to ensure the availability of a generic model that encompasses the essential components of an aircraft, striking a wise balance between simplicity and fidelity to reality.

One illustrative instance of an open-source structural finite element model of a generic aircraft configuration is FERMAT, as documented in Klimmek [1]. The geometric foundation of FERMAT is rooted in the NASA Common Research Model (CRM) [2], similar in size and overall parameters to a long-range wide-body transport aircraft configuration. Notwithstanding its relevance, the CRM's design for $\boldsymbol{Ma}$=0.85 flight introduces complexities, particularly in the transonic regime, where unsteady aerodynamic phenomena, such as shock-induced separation effects, cause nonlinearities and potentially influence flutter boundaries, making it less than ideal for demonstration purposes. Furthermore, it is impossible to tune in some properties or exaggerate some effects to highlight flexibility or flutter mechanism for example.

In parallel, the Active Aeroelastic Aircraft Structures (3AS) project [3], funded by the European Comission (EC), extensively explored active aeroelastic concepts for a group of different classes of reference aircraft: a 4-engine wide body transport aircraft, designated as the EuRAM [4] configuration; a commuter jet aircraft, designated as the X-DIA [5]; and a high aspect ratio – high altitude configuration (HARW) [6]. Regrettably, while the project presented a range of aircraft models, they were exclusively disseminated among project partners, preventing public access to aeroelastic models.

Another open-source aircraft model, integral to the Aeroelastic Prediction Workshop (AePW) [7], emphasizes the evaluation of existing computer codes and modeling techniques. As well, one of the workshop's goal is to identify computational and experimental areas needing additional research and development. The chosen configuration for the workshop, Benchmark Supercritical Wing (BSCW), however, provides only the wing model, and not the entirety of an aircraft model.

Motivated by this noticable absence of an open-source generic aeroelastic model possessing required complexity, the aeroelastic model of the Douglas DC-3 has been meticulously established. This model serves as a demonstrative platform for software testing, including Deutsche Zentrum für Luft- und Raumfahrt (DLR) in-house tool the *Loads Kernel* Software [8] and the commercial software *MSC Nastran* [9]. The *Loads Kernel* Software facilitates the calculation of quasi-steady and dynamic maneuver loads, unsteady gust loads in both time and frequency domains, and dynamic landing loads based on a generic landing gear module. *MSC Nastran*, a Finite Element Analyses (FEA) software, is employed for simulating and analyzing the behavior of structures and mechanical components in engineering applications.

The development of the Douglas DC-3 aeroelastic model addresses the critical knowledge gap by providing a representative and comprehensive model for demonstration and testing purposes. The overall objective is to offer a valuable resource to the broader community, serving as an example and starting point for further developments in this domain. Moreover, this work underscores the pivotal role of Aeroelasticity in Aircraft Design, Performance, and Flight Dynamics and Stability, elucidating

the nuanced interplay between unsteady flow and flexible structures and emphasizing disparities between rigid and flexible aircraft approaches, highlighting aeroelastic phenomena like flutter mechanism, and the resultant variations in experienced loads.

2 Aicraft Selection

To ensure the generality and representativeness of the aeroelastic model, an optimal aircraft was chosen based on specific requirements. The decision involved selecting an existing aircraft and, if needed, introducing modifications to highlight aeroelastic phenomena.

2.1 Aircraft Requirements

The chosen aircraft needed to balance complexity and simplicity while capturing relevant aeroelastic effects. Key criteria included:

- **Configuration:** Simple, conventional.
- **Wing:** Non-rectangular planform, significant LE sweep (Λ_{LE}), washin/washout (Φ), dihedral (Γ), cambered airfoil, and aspect ratio ($\boldsymbol{AR} > 8$).
- **Empennage:** Conventional or T-tail.
- **Control Surfaces:** Ailerons, elevators, rudder; flaps excluded.
- **Engines:** Maximum of two.
- **Flight Regime:** Subsonic ($\boldsymbol{Ma} < 0.6$).
- **Representativeness:** Recognizable, non-glider.
- **Data Availability:** Publicly accessible geometric, aerodynamic, structural, and performance data.
- **Aeroelastic Effects:** Wing bending and torsion, evident flutter mechanism.

2.2 Aircraft Comparison

After carefully reviewing the specifications outlined in Section 2.1, an exhaustive search was conducted to identify an aircraft that meets all the specified criteria. A notable challenge encountered during this search was the prevalence of subsonic aircraft with either no sweep angle or very low sweep angles in their wings. This is attributed to the use of straight wings in subsonic aircraft to enhance lift efficiency and ensure predictable stall behavior at lower speeds, thereby complicating the task of finding an aircraft that satisfies both requirements.

	Dornier 328	**ATR 42**	**Embraer 120**	**Douglas DC-3**
Aircraft Type	commercial	commercial	commercial	commercial/military
Flight Regime	subsonic	subsonic	subsonic	subsonic
Tail Configuration	T-tail	T-tail	T-tail	conventional
N° of Engines	2	2	2	2
Aspect Ratio	11.0	11.1	9.9	9.2
Wing LE Sweep	<5°	<5°	<5°	15.5°
Wing Dihedral	0°	0°	7.5°	5°

Table 1: Aircraft characteristics comparison.

The aircraft comparison in Table 1 showcases various selected options, each either meeting or closely approaching the specified criteria for aircraft selection.

The Douglas DC-3 best met all criteria, particularly regarding wing sweep and data availability. Its historical significance and widespread use further supported this selection.

2.3 Douglas DC-3

The Douglas DC-3 is a low-wing, all-metal monoplane with retractable landing gear. Initially powered by Wright R-1820 Cyclone engines, later versions adopted Pratt & Whitney R-1830 Twin Wasp engines. With a cruise speed of 333 km/h and a range of 2,400 km, it set standards for reliability and efficiency.

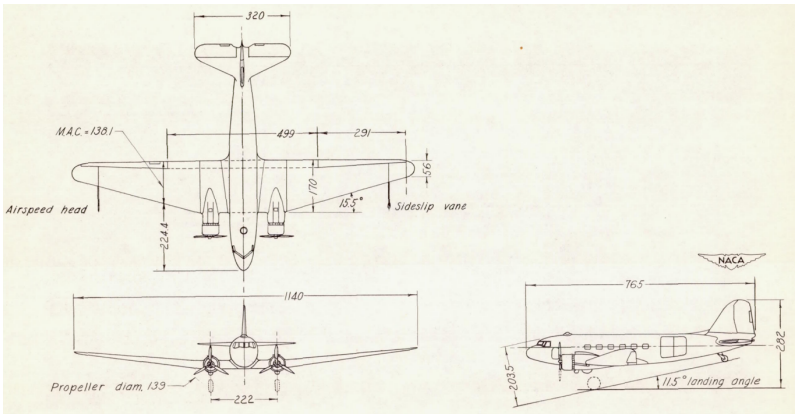

Fig. 1: Three-view drawing of a Douglas DC-3. All dimensions in inches [10].

Key specifications of the DC-3A variant:

General Characteristics:

- **Length:** 19.7 m, **Wingspan:** 29.0 m, **Height:** 5.16 m
- **Wing area:** 91.7 m^2, **Airfoil:** NACA 2215 (root), NACA 2206 (tip)
- **Empty weight:** 7,649 kg, **Max take-off mass:** 11,884.12 kg
- **Engines:** 2 × Pratt & Whitney R-1830, 890 kW each
- **Propellers:** 3-bladed Hamilton Standard 23E50, 3.5 m diameter, constant speed, feathering

Performance:

- **Cruise Speed:** 339 km/h, **Max Speed:** 413 km/h, **Stall Speed:** 125.9 km/h
- **Range:** 2,540 km, **Ceiling:** 7,100 m, **Climb Rate:** 5.8 m/s
- **Wing loading:** 125 kg/m^2, **Power/mass:** 156.5 W/kg

Figure 1 provides visual representations of the aircraft's three views.

3 Aeroelastic Model

3.1 Finite Element Model

The finite element model (FEM) of the Douglas DC-3 was developed using *ModGen*, an in-house tool at DLR designed for generating structural models within *MSC Nastran*. This tool specializes in aircraft components such as wing-like and fuselage structures and allows the definition of input cards for structural optimization and aeroelastic analysis [11].

3.1.1 Planform Definition

The FEM was created for the aircraft's lifting surfaces, including the wings, horizontal tail, and vertical tail. The planform geometry was derived from technical drawings and general aircraft specifications available in [10]. Where precise data were unavailable, dimensions were scaled from the drawings. Control surface geometries were approximated, ensuring that their total areas remained consistent with the reported values. Flaps were excluded for modeling simplicity.

To mitigate numerical issues, rounded tips of lifting surfaces were approximated with straight edges. Key geometric parameters were extracted, such as the wing's dihedral angle (5°) and incidence angle (2°), while the horizontal tail was assumed to have both angles at 0°. A reference point was defined 2 meters ahead of the nose to maintain positive dimensions throughout modifications.

3.1.2 Airfoils

Airfoils were assigned based on available documentation. The wing features a transition from NACA 2215 (root) to NACA 2209 (tip). Since specific airfoil data for the empennage were unavailable, a symmetric NACA 0010 airfoil was selected based on estimated thickness-to-chord ratios from the technical drawings.

3.1.3 Spars and Ribs

Wing spars were defined based on detailed information available in [12], positioning three spars at 17.65%, 38.80%, and 60.00% of the chord. Only the front and rear spars were modeled, with equivalent stiffness properties assigned to account for the omitted central spar. The load reference axis (LRA) was defined along the wingbox centerline.

The horizontal and vertical tails were assumed to have five spars each, evenly spaced. Ribs were distributed along the wingspan, totaling 31 ribs per wing, while the horizontal and vertical tails had eight and nine ribs, respectively. Stringers were not explicitly modeled but their contribution to stiffness was accounted for in the structural properties.

3.1.4 Materials

A single aluminum alloy was assumed for all structural components, considering its common usage in aircraft structures and similar mechanical properties across different alloys. Based on tabulated values for aluminum alloys [13], the material properties

were set as follows: density (ρ) = 2710 kg/m^3, Young's modulus (E) = 70 GPa, shear modulus (G) = 26.9 GPa, and Poisson's ratio (ν) = 0.3.

3.1.5 Structural Model

The lifting surfaces were modeled as beams along the LRA, with stiffness properties manually assigned using *Python* scripts. Each wing consisted of 30 sections between the ribs, where stiffness parameters such as cross-sectional area, moment of inertia, and torsional constants were computed based on spar, skin, and stringer contributions. To account for stringers, an equivalent stiffness method was applied, where their sectional area and moment of inertia were distributed across the wingbox walls. This ensured a realistic representation of their contribution to bending and torsional stiffness.

The structural properties were tuned iteratively to align with expected stiffness distributions derived from historical references and previous aeroelastic studies. The stringer contribution was particularly relevant in adjusting the bending stiffness, as they provide significant reinforcement along the wing span. By incorporating these effects, the model ensures a more accurate prediction of wing deformation and overall dynamic response.

To represent the fuselage, a rigid body approach was adopted to simplify the model while preserving essential dynamic characteristics. A central reference grid point was defined with independent degrees of freedom, whereas dependent degrees of freedom were assigned to 11 grid points along the fuselage length. This method allows for a computationally efficient representation of the fuselage without significantly affecting the overall structural response.

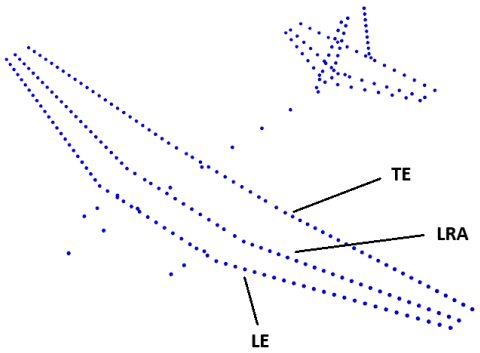

Fig. 2: Douglas DC-3 structural discretization for aeroelastic analyses.

Each engine was discretized into 3 grid points, all rigidly connected to the sixth grid point of the corresponding wing, ensuring a consistent load transfer mechanism between the propulsion system and the lifting surfaces. Similarly, the empennage was

connected to the fuselage through rigid elements, maintaining structural integrity and preventing unrealistic deformations in the model.

Structural mass properties were validated iteratively by adjusting section thicknesses to achieve agreement with estimated component masses from reference data. The final model incorporates accurate mass and stiffness distributions, ensuring reliability in aeroelastic analyses while balancing computational efficiency and model fidelity. The developed structural model serves as a robust foundation for subsequent aeroelastic simulations and dynamic response evaluations. In Figure 2 the structural discretization of the model can be seen.

3.2 Mass Model

The development of the mass model involves three key steps. First, an estimation of the masses of different aircraft components is obtained. Next, the distribution of these estimated masses throughout the aircraft is determined. Finally, fuel modeling is addressed separately due to its additional complexity.

3.2.1 Mass Estimation of Aircraft Components

Statistical weight estimation methods rely on historical data obtained from existing airplanes. By analyzing the wing structure weight of a group of aircraft within a specific class, relationships can be formulated based on geometric parameters such as wing area, aspect ratio, and ultimate load factors. The assumption is that wing weights of aircraft in the same class, certified to the same regulations and with similar gross weights, should exhibit similarities, even if produced by different manufacturers. These methods typically require the establishment of certain dimensions beforehand [14].

The Douglas DC-3, being an aircraft developed and manufactured in the 1930s, adheres to materials and manufacturing techniques consistent with those anticipated by these statistical methods. The equations used for weight predictions are tailored for conventional general aviation aircraft, presuming an aluminum aircraft structure. The methodologies employed draw from the works of Raymer [15], Torenbeek [16], and Anderson [17] from the USAF.

These equations are valid only under specific conditions, requiring careful evaluation before implementation. Engineering judgment was applied to discern and exclude certain equations. The selected methods align with the same class as the Douglas DC-3. The final mass estimation for each component was determined by averaging the valid prediction methods. Methods yielding illogical estimates were excluded.

To validate the results, mass estimations for all components were summed and compared against the empty weight ($\boldsymbol{W_E}$) of the aircraft. If a perfect match was not achieved, a scaling factor was applied. For the DC-3, the estimated weights were 5.7% lighter than the actual empty aircraft weight, necessitating a scaling factor of 1.06. This factor being close to 1 indicates that the mass predictions were accurate.

Table 2 presents the weight mass estimations for various aircraft components, along with the empty mass after the application of the scaling factor. For detailed information about what the different aircraft components include, please consult Gudmundsson et at [14].

Components	Mass [kg]
Wing	1616.3
Horizontal Tail	151.2
Vertical Tail	115.2
Fuselage	1407.8
Installed Engine	1883.8
Landing Gear	310.7
Fuel System	207.1
Flight Control System	241.9
Hydraulic System	12.5
Avionics	142.3
Electrical System	255.9
Air Conditioning	608.0
Furnishings	696.3
Empty aircraft weight	7649.0

Table 2: Weight mass estimations for the different components.

3.2.2 Components Mass Model

After obtaining mass estimations for various aircraft components, their distribution throughout the aircraft was determined, along with their mass moments of inertia.

For wing-like components (wing, horizontal tail, and vertical tail), the total component weight was distributed among the component nodes. The mass was allocated as smaller masses at the LRA nodes, assuming the center of mass of each cross-section lies in the LRA. The distribution process considered the cross-sectional area of different sections. A weighted average method was used for the right and left wing, right and left horizontal tail, and vertical tail, as shown in Equations 1–3.

$$m_i = \frac{m_{wing}}{2} \cdot \frac{A_i}{\sum_{j=1}^{n} A_j} \tag{1}$$

$$m_i = \frac{m_{ht}}{2} \cdot \frac{A_i}{\sum_{j=1}^{n} A_j} \tag{2}$$

$$m_i = m_{vt} \cdot \frac{A_i}{\sum_{j=1}^{n} A_j} \tag{3}$$

For the fuselage, mass distribution was performed over 11 nodes, using a weighted average based on cross-sectional areas, approximated as ellipses. The major and minor axes were derived from technical drawings (Figure 1).

System masses were also distributed, including the landing gear, fuel system, flight control system, hydraulic system, avionics, electrical systems, air conditioning, and furnishings. The landing gear mass was partitioned into three locations, corresponding to the main and rear landing gears. Mass distribution followed Gudmundsson et al. [14]. Fuel system masses were allocated to locations near the fuel tanks, ensuring alignment with documented aircraft center of mass positions [12]. The mass moments of inertia were also calculated for each component, providing critical data for aeroelastic and dynamic analyses. Figure 3 illustrates the mass modeling of the Douglas DC-3.

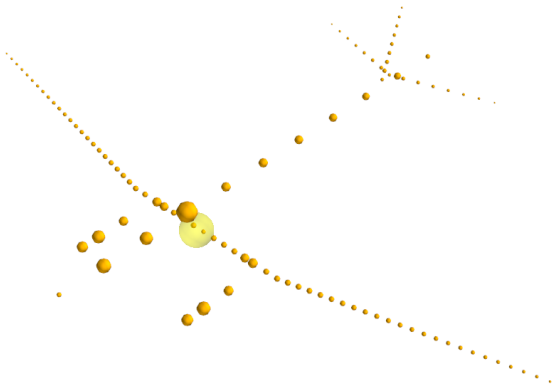

Fig. 3: Douglas DC-3 mass modeling, including structural, systems, crew, and standard equipment masses.

3.2.3 Fuel Model

Fuel modeling is complex due to its significant mass and inertia properties. Fuel masses were discretized per fuel bay and modeled as volume elements to obtain inertia properties and filling levels. The fuel model was developed using the DLR in-house tool *ModGen*, requiring the definition of fuel tank geometry. Initially, five fuel tanks per wing were considered but later reduced to four to achieve a more realistic utilization factor of 0.7864. Figure 4 illustrates the full fuel tanks model for the right wing.

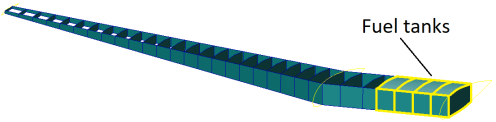

Fig. 4: Douglas DC-3 right wing full fuel tanks.

3.3 Aerodynamics Model

The aerodynamic model was developed using the Doublet Lattice Method (DLM). This approach requires the construction of an aerodynamic mesh composed of quadrilateral panels. While the DLM enables modeling of control surface motions, its accuracy in capturing control surface effects is influenced by discretization, often necessitating empirical corrections [18]. To ensure accuracy, the meshing process must be performed rigorously. The aerodynamic mesh was generated using *ModGen*.

The aerodynamic mesh comprises macro panels for the wing, horizontal tail, and vertical tail, ensuring proper resolution of aerodynamic loads. Proper alignment between the wing and horizontal tail panels was maintained, ensuring that

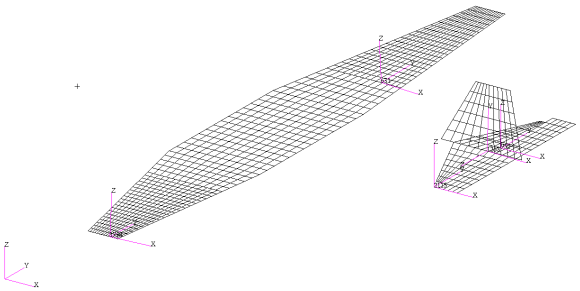

Fig. 5: Douglas DC-3 model aerodynamic mesh.

each wing panel corresponds to only one horizontal tail panel to prevent numerical inconsistencies. Figure 5 presents the final aerodynamic mesh for the Douglas DC-3 model.

3.4 Mass Configurations

Testing different mass configurations is crucial for aircraft development and certification. It helps evaluate structural integrity, fuel efficiency, and compliance with regulatory standards, while also being essential for load, gust, and flutter analyses. For this study, four representative mass configurations were selected for the Douglas DC-3, as summarized in Table 3.

Mass configuration	Fuel	Payload	
M1	0%	0%	OEM
M2	100%	0%	Max Range
M3	49%	100%	MTOM
M4	0%	100%	-

Table 3: Mass configurations.

The mass configurations are defined as follows:

- M1 (OEM): Operational Empty Mass, consisting of structure, crew, and standard equipment.
- M2 (Max Range): Maximum range configuration, adding full fuel to the OEM.
- M3 (MTOM): Maximum Take-Off Mass, combining 49% of fuel capacity with the maximum payload.
- M4: OEM with maximum payload, excluding fuel.

3.5 Modified Models

The original model of the Douglas DC-3 was found to fall short of the required performance, particularly regarding aeroelastic effects. This section presents four modified models with adjusted stiffness and inertial properties, which were analyzed based on

trim conditions for horizontal flight at a Load Factor of $n_Z = 1$, True Airspeed (TAS) of 70 m/s, and Flight Level FL000. The M3 mass configuration was used for these tests due to its significant structural deformations, representing a critical test case.

	α_{trim} [deg]	η_{trim} [deg]	C_L	$C_{L_{cs}}$	C_{L_f}	C_{L_f}/C_L
Original	1.39	0.83	0.423	-0.008	-0.003	-0.7%
More Flex 1	1.52	0.90	0.423	-0.009	-0.015	-3.5%
More Flex 2	1.53	0.90	0.423	-0.009	-0.016	-3.8%
More Flex 3	1.60	1.10	0.423	-0.011	-0.020	-4.7%
More Flex 4	1.46	0.69	0.423	-0.007	-0.011	-2.6%

Table 4: Trim results for different aeroelastic models for M3.

Table 4 summarizes the trim results for the four models. For the original model, the elastic deformation contributed negligibly to the lift coefficient. In contrast, modifications to wing stiffness and mass properties in the "More Flex" models led to greater contributions from elastic deformations, ranging from 2.6% to 4.7%.

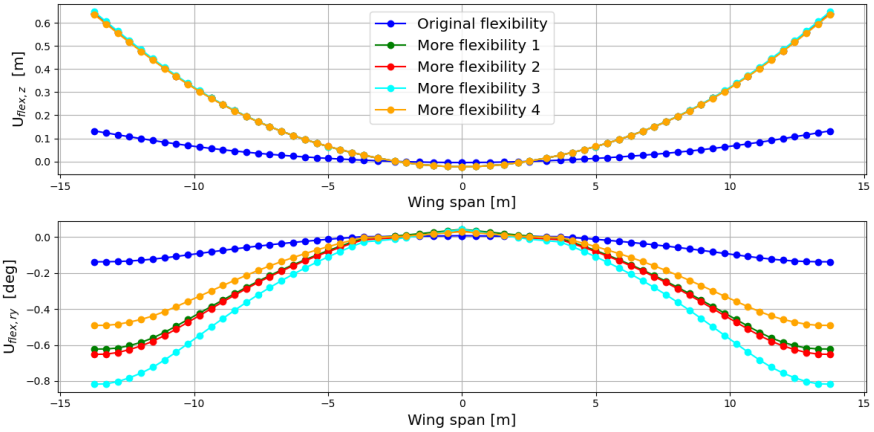

Fig. 6: Elastic deformation of the main wing at Load Factor of $n_Z = 1$, with a True Airspeed (TAS) of 70 m/s, Flight Level FL000, and M3 mass configuration for the original and modified aeroelastic models.

The "More Flex" models were adjusted by reducing the wing's stiffness properties, as shown in the trim and deformation results. Figure 6 illustrates the elastic deformation of the wing for each model. The vertical displacement at the wing tip increased from $U_{flex,Z} = 0.13$ m in the original model to $U_{flex,Z} = 0.64$ m in the first modified model. Elastic twist also grew significantly, reaching $U_{flex,ry} = -0.62$ degrees in the first modified model.

In the third and fourth modified models, the location of the wing's Elastic Axis (LRA) was varied to assess the impact on aeroelastic behavior. The third model, with a

forward LRA, showed a 4.7% contribution of elastic deformation to the lift coefficient, while the fourth, with an aft LRA, had a 2.6% contribution. The twist deformation at the wing tip was larger in the third model ($U_{flex,ry} = -0.82$ degrees) compared to the fourth model ($U_{flex,ry} = -0.49$ degrees), demonstrating that a forward LRA amplifies aeroelastic effects.

These results highlight the increased role of aeroelasticity as the stiffness is reduced and the LRA is adjusted. The third modified model exhibits the greatest aeroelastic influence.

3.6 Eigenmodes

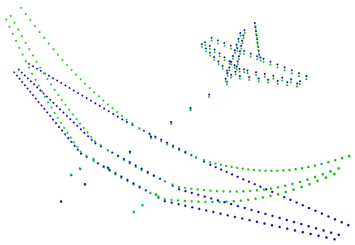

(a) First symmetric wing bending, f=3.17 Hz

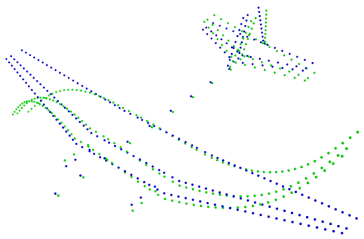

(b) First antisymmetric wing bending, f=4.72 Hz

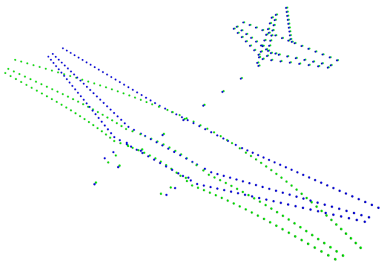

(c) First symmetric in-plane wing bending, f=7.26 Hz

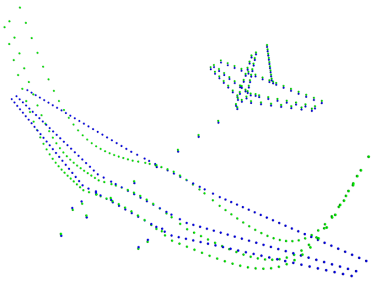

(d) Second symmetric wing bending, f=8.00 Hz

Fig. 7: First four flexible mode shapes for the M3 mass configuration.

Eigenmodes and eigenfrequencies of the final modified aeroelastic model were computed using *Loads Kernel*, with results also validated via *MSC Nastran* (SOL103). For visualization, *Model Viewer* was employed.

The first six eigenvalues, corresponding to the rigid body modes, were close to zero Hz, as expected. The first four flexible mode shapes for the M3 mass configuration are shown in Figure 7. Notably, the first eigenmode has a frequency of 3.17 Hz, which does

not fall in the range expected from an aircraft of the size and weight of the Douglas DC-3, reflecting the model's tuning. Importantly, a distinct pure wing torsion mode appears at 9.60 Hz (seventh eigenmode), which was a desired outcome. Additionally, several modes exhibit coupling between wing bending and torsion.

4 Results

4.1 Trim Cases

Using the mass and stiffness matrices from *MSC Nastran*, the trim conditions for the Douglas DC-3 model were computed using both *Loads Kernel* and *MSC Nastran* (*SOL 144*). Three trim cases were analyzed at a True Airspeed (TAS) of 70 m/s and Flight Level FL000: horizontal level flight ($n_Z = 1$), a push-down maneuver ($n_Z = -1$), and a pull-up maneuver ($n_Z = 2.5$). These cases were selected based on the aircraft's flight envelope, following CS-25 certification specifications [19].

The trim results showed close agreement between both software tools, with only minor differences attributed to their modeling approaches. *Loads Kernel* employs a modal approach requiring a convergence study, which indicated that 71 eigenmodes were sufficient for accurate results. Additionally, *MSC Nastran* assumes no elastic deformation at the wing root, whereas *Loads Kernel* allows for it, making direct comparisons in the flexible case more complex.

Comparing the rigid and flexible configurations highlights the significant impact of aeroelasticity. For instance, in horizontal level flight, *Loads Kernel* results indicate a 26.6% difference in trim angle of attack due to flexibility, demonstrating the necessity of considering aeroelastic effects in flight performance, stability, and control analyses.

Table 5 presents the contribution of flexibility to total lift, revealing a negative effect. In horizontal level flight, flexibility reduces lift by 5.22%. This phenomenon is linked to the elastic deformation of the wing, as analyzed further below.

	Loads Kernel	
	Rigid	**Flexible**
n_Z=1	0	-5.22%
n_Z=-1	0	-2.03%
n_Z=2.5	0	-4.77%

Table 5: Trim cases $\frac{C_{L_f}}{C_L}$ results for the final modified model, for M3.

Further illustrating the role of aeroelasticity, Figure 8 depicts the elastic deformations of the wing along the span for each trim case. The vertical displacement $U_{flex,Z}$ follows the expected trends: upward bending in level flight and pull-up maneuvers, and downward bending in push-down maneuvers. The most pronounced displacement occurs during pull-up maneuvers, reaching 1.55 m at the tip (10.7% of the half-span), which remains within the validity limits for linear elasticity assumptions.

Elastic twist $U_{flex,ry}$ also exhibits significant variation, particularly at the wing tip. In level flight and pull-up maneuvers, a nose-down twist is observed in the outer wing section, while the inner section experiences a slight nose-up twist. The opposite trend is noted during push-down maneuvers. The maximum elastic twist of -1.98 degrees at the wing tip significantly alters the lift distribution along the wing, influencing overall performance.

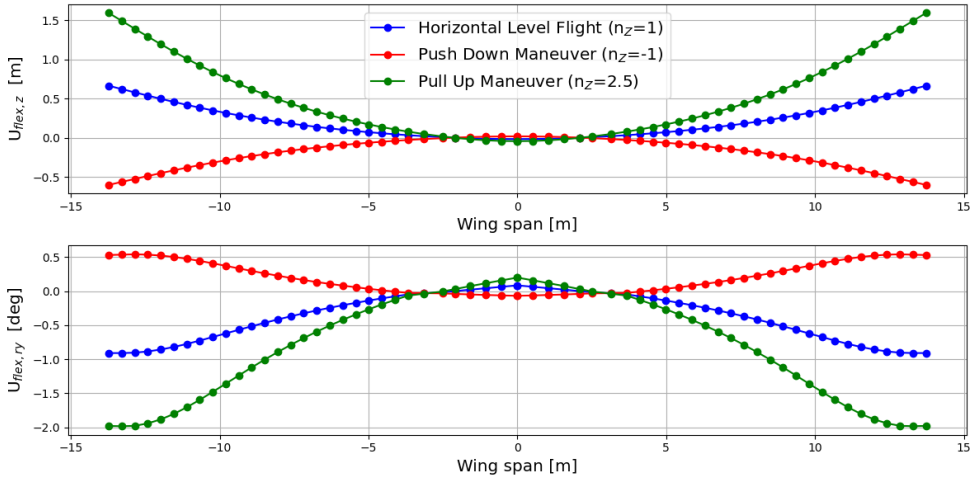

Fig. 8: *Loads Kernel* elastic deformation of the main wing at certain speed, M3 for the final modified aeroelastic model.

4.2 Maneuver Loads

Maneuver loads are a key factor in sizing an aircraft's primary structure. The selected load cases follow CS-25 regulations, including horizontal level flight (n_Z = 1), push-down (n_Z = -1), pull-up (n_Z = 2.5), and roll maneuvers. The roll rate derived from CS-25 Amendment 28 [19] is 5.45°/s, but to yield more representative loads, a roll rate of 20°/s over 3 seconds was used. All cases were analyzed at a True Airspeed (TAS) of 70 m/s at Flight Level FL000.

The *Loads Kernel* was used to derive section loads from integrated nodal loads at 16 monitoring stations per wing. The main quantities of interest are bending moment M_x, torsional moment M_y, and shear force F_z. Given the validated agreement with *MSC Nastran* (Section 4.1), only *Loads Kernel* results are presented.

Figure 9 illustrates the spanwise envelopes of M_x, M_y, and F_z. As expected, for the left wing (negative y values) the pull-up maneuver (number 3) produces the highest negative bending moment at the root, while the push-down maneuver (number 2) induces the highest positive bending moment. The torsional moment M_y trends reveal an inversion of the critical load case near the wing kink, influenced by elastic twist deformation (Figure 8). Roll maneuvers contribute significantly to torsional loads in

the outboard section. The shear force F_z follows a similar pattern to M_x, but peaking in a section near the root and not in the root.

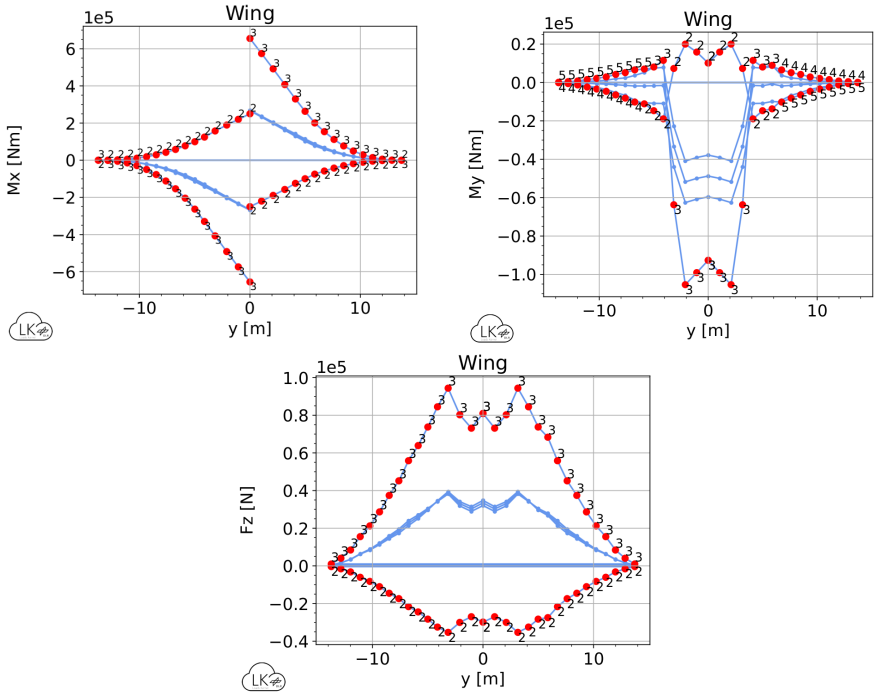

Fig. 9: Envelope of bending moment M_x, torsional moment M_y, and shear force F_z along the wing span.

To identify critical load cases, two-dimensional load envelopes were evaluated. Figure 10 presents the M_x-M_y interaction at the wing root and just after the wing kink. The root experiences the highest loads due to the structural attachment to the fuselage. At the wing root, the pull-up maneuver yields the maximum negative bending moment, while the push-down maneuver results in the highest positive moment. The roll maneuvers introduce an offset in M_y compared to horizontal level flight, reflecting increased elastic twist. At the wing kink there is a inversion in M_y. This discrepancy stems from the observation made in the previous section (Figure 8), where the elastic twist $U_{flex,ry}$ of the outboard wing section after the kink becomes negative (nose-down torsional twist). Furthermore, the roll maneuvers exhibit a larger offset compared to horizontal level flight, transforming the shape of the envelope from an elongated rhombus to a bulkier one.

4.3 Gust Loads

To analyze gust loads, the (1-cos) Discrete Gust Model was implemented in *Loads Kernel*. The gust analysis was conducted under the same conditions as the maneuver

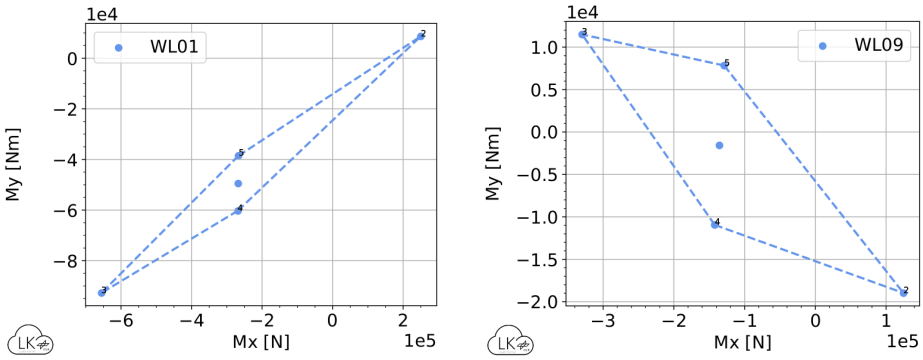

Fig. 10: Load envelope of bending moment M_x and torsional moment M_y at the wing root (left) and just after the wing kink (right).

loads, at a True Airspeed (TAS) of 70 m/s and Flight Level FL000 at trim conditions. In compliance with CS-25.341 [19], the gust profiles at sea level were obtained. Table 6 lists the corresponding gust gradients and peak velocities, ensuring that the spectrum required by certification specifications was adequately covered.

Gust gradient [m]	**9**	**16**	**23**	**30**	**37**	**51**	**65**	**79**	**93**	**107**
Peak velocity [m/s]	10.4	11.4	12.1	12.7	13.1	13.8	14.4	14.9	15.3	15.6

Table 6: Gust gradients and corresponding peak velocities.

One-dimensional and two-dimensional load envelopes were analyzed similarly to maneuver loads. Given their comparable magnitudes and shapes, the primary focus is placed on the time-domain response of the forces and moments.

Figure 11 presents the bending moment M_x over time for different gust gradients at the wing root and wing kink. The magnitudes of the positive and negative peaks are similar, which was unexpected. The highest positive peak occurs for a gust gradient of $H = 23$ m, differing from empirical predictions [20], which indicate that the highest excitation should occur around $H = 44$ m.

Figure 12 illustrates the shear force F_z over time, revealing similar trends to M_x. The torsional moment M_y over time (Figure 13) shows that negative peaks are larger than positive ones, with the highest negative peak arising from $H = 9$ m. Notably, in the wing kink section (Figure 13b), oscillations with significant amplitude appear for $H = 9$ m, likely indicating the excitation of an eigenmode with a frequency of approximately 3.3 Hz, close to the first symmetric wing bending mode (3.17 Hz). But, these oscillations are seen in the torsional moment M_y plot. The possible justification is that the torsional stiffness is much lower compared to the bending stiffness, and on top of that the wing mass points are located far aft of the LRA, which creates a strong bending and torsional coupling.

In order to get to the sources of these unexpected results: the negative and positive peaks having the same size and the highest peak not correspond to the gust gradient

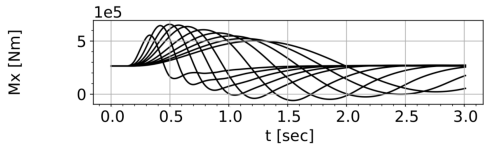

(a) Wing root.

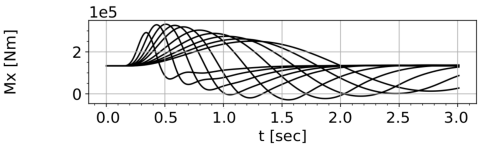

(b) Wing kink.

Fig. 11: Bending moment M_x over time for different gust gradients.

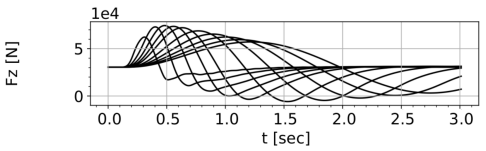

(a) Wing root.

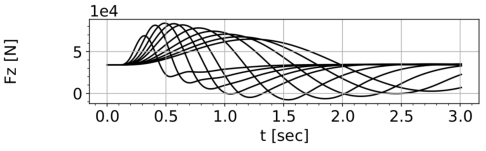

(b) Wing kink.

Fig. 12: Shear force F_z over time for different gust gradients.

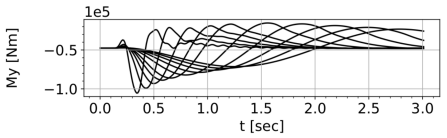

(a) Wing root.

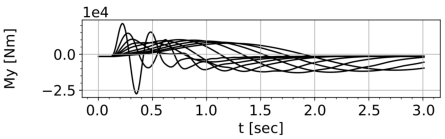

(b) Wing kink.

Fig. 13: Torsional moment M_y over time for different gust gradients.

expected, some extra simulations were performed. It was discovered a coupling between the gusts and one of the longitudinal flight mechanics modes, the short period. One way to eliminate this coupling is to decreased the distance between the aerodynamic center and the center of gravity, so the static margin. The aircraft model has a very high static margin in the M3 mass configuration, which was reduced to approximately 10%. This resulted in changes in the magnitude of the positive and negative peaks of the moments/forces over time plots, so that the magnitude of these positive and negative peaks was then much different between them. On top of that, the highest peak was then arising from a gust with a gust gradient between H = 37 m and H = 51 m. This means the empirical predicted gust gradient value of H = 44 m falls in this range. This goes to show that the unexpected gust load results obtained are justified by this gust and short period coupling that happens for gust profiles with small gust gradients.

4.4 Flutter Check

In the aerospace industry, flutter analysis ensures the safety and structural integrity of aircraft by identifying potentially dangerous oscillations caused by the interaction of aerodynamic forces and structural dynamics. Conducting a flutter check helps assess potential flutter conditions and enables necessary design modifications.To perform the

flutter check, both *Loads Kernel* and *MSC Nastran* SOL145 were used. The analysis was conducted at FL000 (where Equivalent Airspeed = True Airspeed) with the M3 mass configuration. The pk-method was employed for both checks.

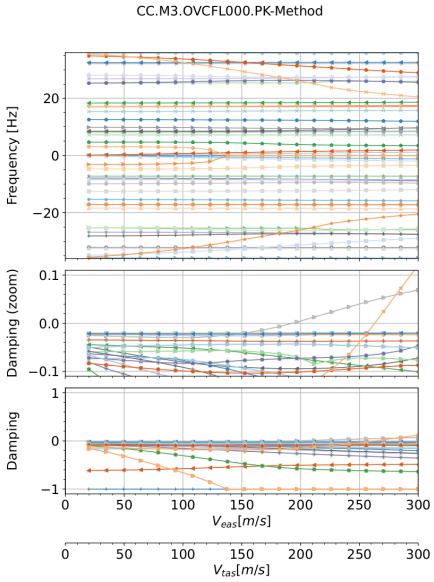

Fig. 14: Flutter results *Loads Kernel*.

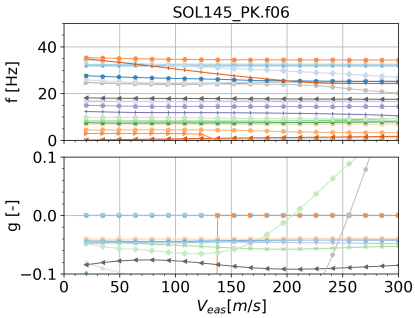

Fig. 15: Flutter results *MSC Nastran*.

Figure 14 shows the flutter results for *Loads Kernel*, with a frequency plot indicating the variation of each eigenmode's frequency with velocity, and a damping plot showing eigenmode damping. At 195 m/s, the first mode becomes unstable ($V_{flutter}$ = 195 m/s, M = 0.569). That is the symmetrical pure torsion mode. The second mode becomes unstable at 262 m/s, with a frequency decrease from 36 Hz to 23 Hz.

In Figure 15, the *MSC Nastran* results show a similar trend. The first mode becomes unstable (correspponding to the symmetrical pure torsion mode) at 203 m/s ($V_{flutter}$ = 203 m/s, Ma = 0.592), and the second mode at 256 m/s, with a frequency decrease from 26.19 Hz to 23 Hz. Both methods exhibit a similar final instability frequency of 23 Hz. Both flutter speeds are outside the flight envelope (V_{NE} = 119.72 m/s), but within the subsonic regime ($\boldsymbol{Ma} < 0.6$).

5 Conclusion and Outlook

This work develops the Douglas DC-3 aeroelastic model, bridging the identified knowledge gap with a comprehensive and open-source model for demonstration and testing. Tutorials and additional details are available here and here. The model, which balances complexity and simplicity, underscores the importance of aeroelasticity in aircraft design and stability.

The DC-3 model features a conventional configuration, including a wing with a leading-edge sweep angle of $\Lambda_{LE} = 15.5°$, dihedral $\Gamma = 5°$, aspect ratio $AR = 9.2$, and a cambered airfoil. The model exhibits wing bending and torsion, with flutter coupling bending and torsion modes. The development included creating finite element and aerodynamic models, along with a fuel mass model via *ModGen*. Four mass configurations were considered: OEM, maximum range, MTOM, and OEM with maximum capacity excluding fuel. The first eigenmode of the final model has an eigenfrequency of 3.17 Hz, due to significant tuning.

Trim case analyses were conducted with *Loads Kernel* and *MSC Nastran* SOL144 for three cases at TAS = 70 m/s and varying load factors. Results matched well, with flexibility reducing the lift coefficient by -5.22% in horizontal level flight. Loads were integrated at monitoring stations to derive section loads, and critical load cases were identified using two-dimensional and one-dimensional load envelopes. Gust loads were studied with the (1-cos) Discrete Gust Model, revealing coupling with the short period mode due to the model's high static margin. A flutter check showed good agreement between *Loads Kernel* and *MSC Nastran*, with flutter speeds of 195 m/s and 203 m/s, respectively, both showing instability in the symmetrical pure torsion mode, demonstrating the similarity in results obtained from both softwares.

Future work could focus on a variety of analyses, including investigations into control surface effectiveness, aeroelastic derivatives, longitudinal stability, and continuous turbulence. Furthermore, to validate these results, high-fidelity methods like Computational Fluid Dynamics (CFD) can be employed.

References

[1] Klimmek, T.: Parametric Set-Up of a Structural Model for FERMAT Configuration for Aeroelastic and Loads Analysis. ASDJournal (2014), Vol. 3, No. 2, 31–49 (2014)

[2] Rivers, M.B.: NASA Common Research Model: A History and Future Plans. NASA Langley Research Center, Hampton, VA 23681

[3] Schweiger, J., Suleman, A., Kuzmina, S., Chedrik, V.: Mdo concepts for an european research project on active aeroelastic aircraft (2002) https://doi.org/10.2514/6.2002-5403

[4] Kuzmina, S., Ishmuratov, F., Zichenkov, M., Chedrik, V.: Integrated numerical and experimental investigations of the active/passive aeroelastic concepts on the european research aeroelastic model euram. ASD Journal **2**(2), 31–51 (2011)

[5] Ricci, A., Scotti, A., Cecrdle, J., Malecek, J.: Active control of three-surface aeroelastic model. Journal of Aircraft **45**(3), 1002–1013 (2008)

[6] Heinze, S.: Aeroelastic concepts for flexible wing structures. PhD thesis, KTH, Royal Institute of Technology (2005)

[7] Heeg, J., Chwalowski, P., Kuzmina, S., Schuster, D.M.: Plans and example results for the 2nd aiaa aeroelastic prediction workshop (2015)

[8] Voß, A.: Loads Kernel User Guide Version 1.04s. Deutches Zentrum für Luft und Raumfahrt, Institute of Aeroelasticity, Göttingen, 136, (2020). Deutches Zentrum für Luft und Raumfahrt, Institute of Aeroelasticity, Göttingen, 136

[9] MSC.Software Corporation: MSC Nastran 2023.1 Quick Reference Guide. (2023). MSC.Software Corporation

[10] Assadourian, A., Harper, J.A.: Determination of the Flying Qualities of the Douglas DC-3 Airplane. Report. https://digital.library.unt.edu/ark:/67531/metadc56979/ Accessed 2024-02-26

[11] Klimmek, T.: ModGen User's Manual. (2023). Version 2023-01-17

[12] QuebecAir Corporation: QuebecAir DC-3 Manual. QuebecAir Corporation, (1957). QuebecAir Corporation. Manual

[13] The Engineering ToolBox: Properties of Aluminum Pipe. https://www.engineeringtoolbox.com/properties-aluminum-pipe-d_1340.html. Accessed: 2024-07-17 (2024)

[14] Gudmundsson, S.: General Aviation Aircraft Design: Applied Methods and Procedures, 2nd edn. William Andrew Publishing, ??? (2022)

[15] Raymer, D.: Aircraft Design: A Conceptual Approach. AIAA Education Series, ??? (1996)

[16] Torenbeek, E.: Synthesis of Subsonic Aircraft Design, 3rd edn. Delft University Press, ??? (1986)

[17] Anderson, R.: Weight Estimation Methods. Unpublished Notes, Design Branch, Air Force Flight Dynamics Laboratory (1973)

[18] Albano, E., Rodden, W.: A doublet-lattice method for calculating the lift distribution on oscillating surfaces in subsonic flow. AIAA Journal **2**(7), 279–285 (1969)

[19] European Union Aviation Safety Agency (EASA): Certification Specifications and Acceptable Means of Compliance for Large Aeroplanes (CS-25). (2007). European Union Aviation Safety Agency (EASA)

[20] Donley, P.: Summary of information relating to gust loads on airplanes. Technical report, Langley Research Center, NACA, Hampton, Virginia (1950)